.

Impact of excitation pulse width on the upconversion luminescence lifetime of $NaYF_4:Yb^{3+},Er^{3+}$ nanoparticles

Electronic Supplementary Information (ESI)

Alejandro Casillas-Rubio,[a] Diego Mendez-Gonzalez,[b] Marco Laurenti,[b] Jorge Rubio-Retama,[b] Oscar G. Calderón,*[a] and Sonia Melle,*[a]

Contents

[a] *Department of Optics, Complutense University of Madrid, E-28037 Madrid, Spain*
[b] *Department of Chemistry in Pharmaceutical Sciences, Complutense University of Madrid, E-28040 Madrid, Spain*

S1. High resolution transmission electron microscopy (HR-TEM) characterization.

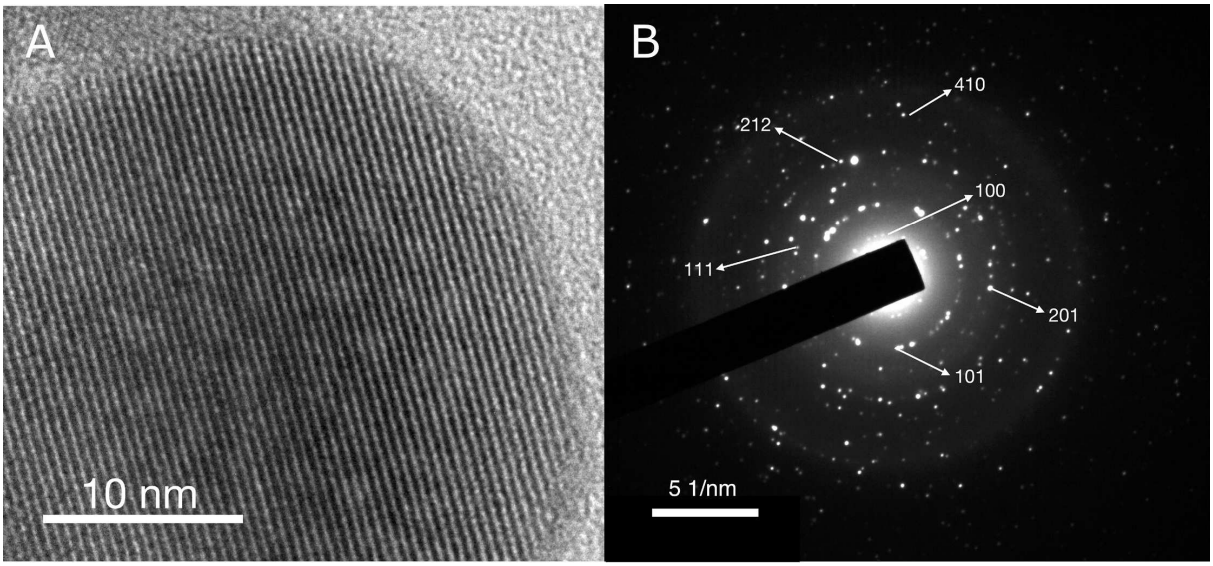

Fig. S1.A) HR-TEM magnification of an oleate-capped UCNP, showing the 100-lattice plane from $NaYF_4$ hexagonal phase. B) Selected Area Electron Diffraction (SAED) pattern from oleate-capped UCNPs. Planes 100 (d = 0.515 nm), 101 (d = 0.290 nm), 111 (d = 0.227 nm), 201 (d = 0.207 nm), 212 (d = 0.130 nm) and 410 (d = 0.112 nm) from $NaYF_4$ hexagonal phase are easily identified, confirming that $NaYF_4$ is in its hexagonal phase according to the JCPDS 16-0334 diffraction card.

S2. Excitation pulse widths and repetition frequencies.

In the following table, we present the various laser pulse widths used in our experiments. For each pulse width, we selected the excitation pulse repetition frequency to ensure relaxation of the ions to the ground level before initiating the subsequent excitation pulse to avoid pile-up effects.[1] Therefore, we employed the minimum frequency provided by our excitation laser controller (ILX Lightwave, model LDX36025-12) for each excitation pulse width. The repetition frequencies are outlined in the following table.

Table 1 Values of the laser pulse widths, repetition frequencies, periods, and duty-cycles used for excitation.

pulse width (μs)	40	100	200	500	750	1000	1000	2000	3000	5000	10000
repetition frequency (Hz)	125	50	25	10	6.6	5	200	100	66.6	40	20
period (ms)	8	20	40	100	150	200	5	10	15	25	50
duty cycle (%)	0.5	0.5	0.5	0.5	0.5	0.5	25	20	20	20	20

The laser controller enables us to select two different pulse modes; a "Pulse mode" for shorter pulse widths (from 40 μs to 1 ms) and a "Hard-Pulse mode" for longer pulse widths (from 1 ms to several ms). As seen in the table, the laser is turned off for more than 10 ms for most of the pulse widths used. Therefore, the ions have ample time to relax to their ground state before a new pulse arrives. For the case of 1 ms pulse width, we conducted two measurements using both pulse modes. Both measurements yielded very similar lifetime values, as evidenced by the experimental data presented throughout the manuscript.

S3. Fitting the UCL decay curves.

We attempted to fit the UCL decay curves using a combination of exponential functions as follows:

$$I_{UCL} = I_0 + A_1 \exp(-(t-t_0)/\tau_1) + A_2 \exp(-(t-t_0)/\tau_2) - A_{rise} \exp(-(t-t_0)/\tau_{rise}) \,. \quad (S1)$$

We considered two decay times, τ_1 and τ_2, along with a rise time τ_{rise} to address the initial moments when the laser is turned off, and the upconversion through energy transfer continues to unfold. Consequently, we calculated the UCL lifetime as an average of the two decay times, weighted by their respective amplitudes A_1 and A_2:

$$\tau_{UCL} = \frac{A_1\tau_1 + A_2\tau_2}{A_1 + A_2} \,. \quad (S2)$$

We plotted in Figure S2A-C the UCL decay curves and their respective fitting curves for three different laser pulse widths. The corresponding lifetime values were represented by colored spheres in Figure S2D. They are in agreement with the values derived from the procedure outlined in Section 2.3.2 of this work, which are also plotted in Figure S2D (data from Figure 2D).

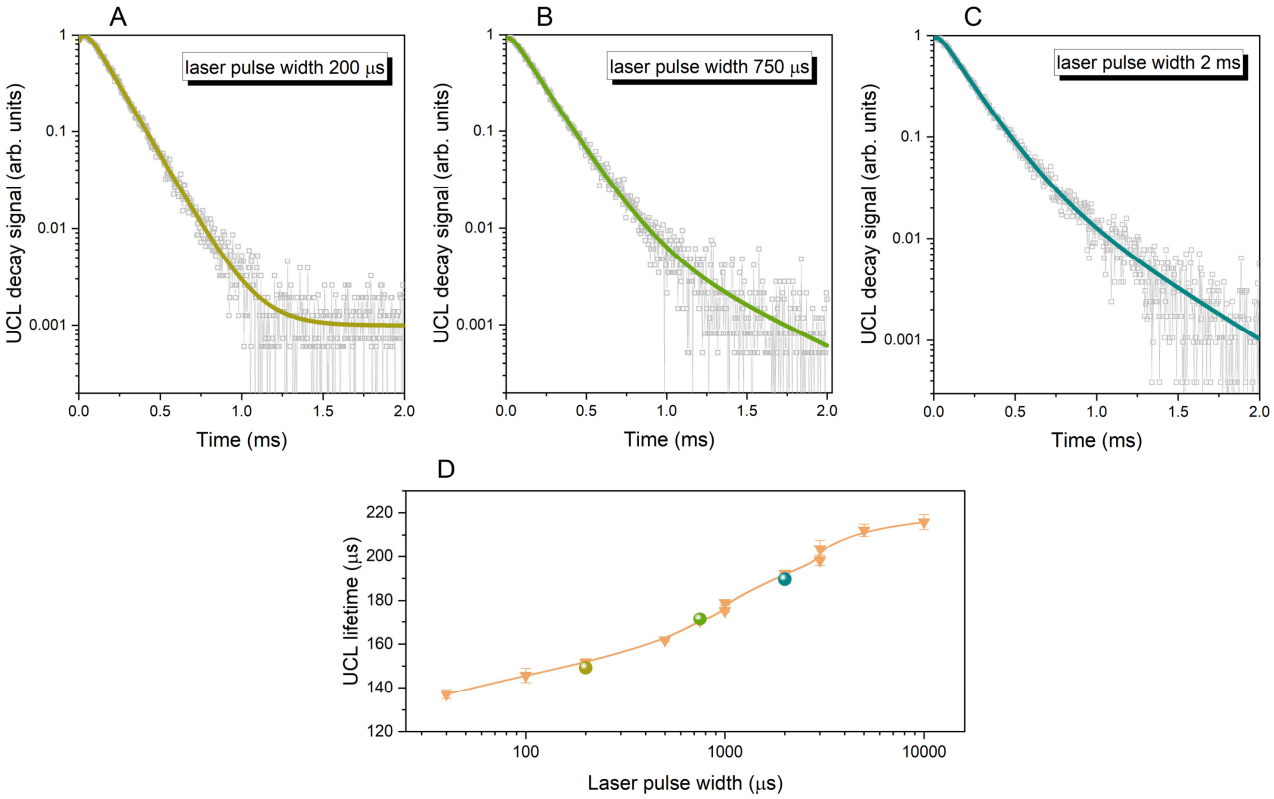

Fig. S2. (A-C) Fitted curves using Equation S1 (solid lines) applied to the UCL decay curves (symbols) for different excitation pulse widths at a laser power of 0.65 W. (D) The UCL lifetime plotted against the laser pulse width, with results obtained through multi-exponential fitting (colored spheres) using Equation S1 and through the procedure explained in Section 2.3.2 (orange triangles).

S4. UCL lifetime at different temperatures.

To verify that this phenomenon is not influenced by temperature-related factors, we performed time-resolved luminescence experiments employing a cuvette holder under precise temperature control (see experimental setup in Figure S3A). Subsequently, we measured the decay curves of UCL, varying the laser pulse width at two distinct temperatures: 20 °C and 40 °C. At both temperatures the behavior of the UCL lifetime is the same, as depicted in Figure S3B. The increase of temperature provokes an enhancement of nonradiative decay rates which leads to a slightly decrease in the UCL lifetime. However, the change in the lifetime due to the laser pulse width is almost the same for both temperatures. This is evident in Figure S3C, where the alteration in UCL lifetime, relative to the value at the shortest laser pulse width, is graphically represented as a function of the laser pulse width.

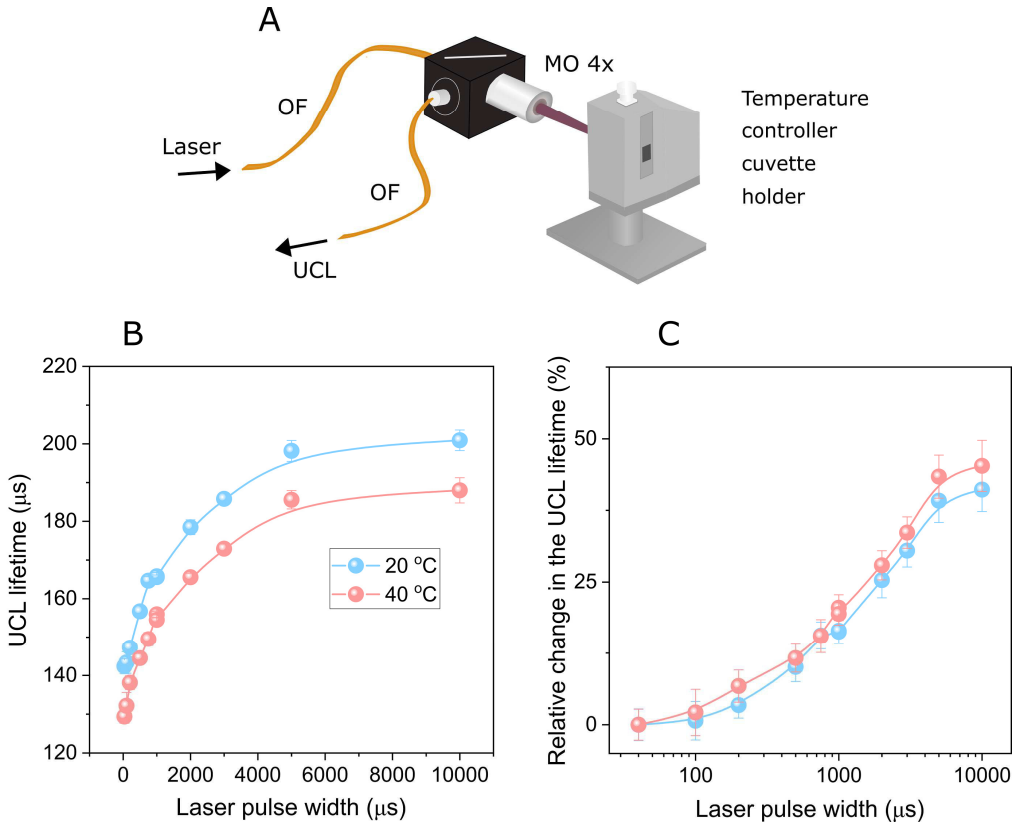

Fig. S3. (A) Scheme of the temperature-controlled cuvette holder with the excitation and emission optical fibers (OF) and the 4x microscope objetive (MO). (B) The UCL lifetime versus the excitation pulse width for two temperatures: 20 and 40 °C. (C) The change in the UCL lifetime versus the pulse width relative to the value obtained at the shortest pulse width, using the data from graph B. The laser power was 2.2 W.

S5. Laser beam diameter measurement.

We have characterized the laser beam profile measuring its section radius with the knife-edge technique at different distances from the microscope objective (11 mm, 12 mm, 13 mm and 19 mm in Figure S4A). On the set up used for the lifetime studies, we place a blade perpendicularly to the direction of the laser beam propagation in a fixed position and, just behind it, a power sensor (Figure S4B). Beginning with the laser beam utterly blocked, the power sensor should indicate values close to zero. Making use of a translation stage manipulated by a micrometer screw, we remove the blade from the beam path, resulting in a continued increase in the power indicated by the sensor. When the blade has completely exited the laser beam path, the power reach a plateau. In this situation, we must ensure that the whole laser beam fall within the power sensor. If we plot power data against the blade position X, curves as in Figure S4A are obtained. This data is fitted to the expression below:

$$P = P_0 + \frac{A}{2}\left[1 + \mathrm{erf}\left(\frac{X - X_C}{w_0}\right)\right], \tag{S3}$$

where P_0 is the minimum power measured, A is the maximum amplitude of power values, and the error function (erf) depends on the central position (X_C) and the beam radius (w_0) measured at a position where the power decreases to $1/e$ times its maximum value. All this information at different positions Z from the microscope objective allows to define laser beam profile and calculate its waist (position and radius) and its Rayleigh length (Z_R):

$$w(Z) = w_0\sqrt{1 + \left(\frac{Z}{Z_R}\right)^2}. \tag{S4}$$

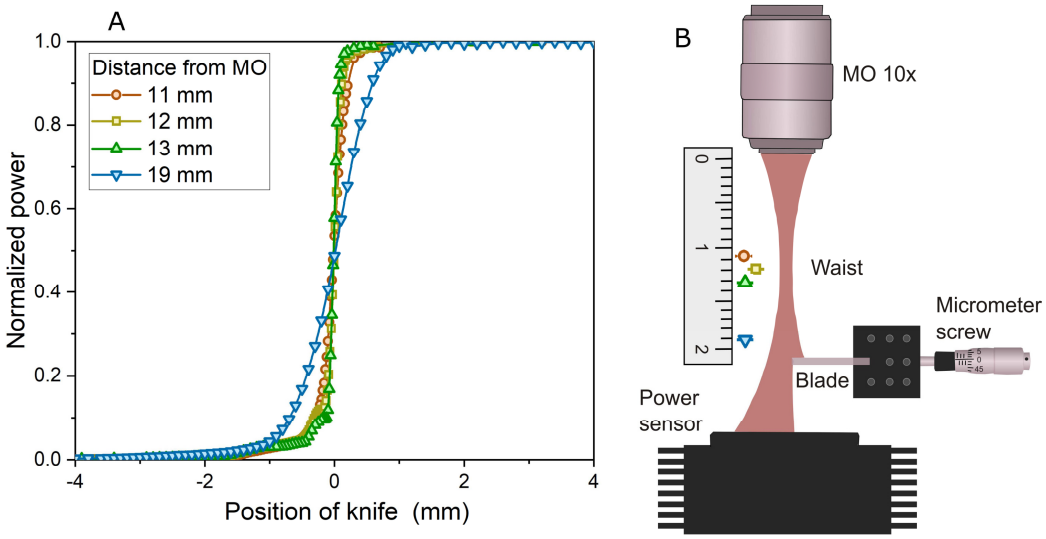

Fig. S4. (A) Profiles of laser beam section at several distances from the microscope objective (11mm, 12 mm, 13 mm and 19 mm) (B) Scheme of set up for knife-edge method with the laser beam leaving the microscope objective (MO),a part of it is blocked by the blade guided by a micrometer screw and the rest reach the power sensor.

S6. Parameter values used in the theoretical model.

The parameter values employed in the theoretical model closely align with those reported in the literature.[2–5]. Furthermore, some of them were utilized as control parameters to accurately replicate the experimental results. Er^{3+} ions in the metastable level 1 ($^4I_{13/2}$) (see Fig. 3A) radiatively decay to the ground state $^4I_{15/2}$ with a decay time of $1/W_{Er1} = 4$ ms. This value was validated by measuring the decay curve for the NIR emission band at 1522 nm, corresponding to the metastable level $^4I_{13/2}$, by exciting the UCNPs with a 10 ms pulse width and 0.65 W. By fitting this decay curve to an exponential decay, we obtained a lifetime of 3 ms. This measured lifetime may be affected by the cross-relaxation between Er^{3+} ions with coefficient C_{Er1}, which depopulates this state, although a strong effect is not expected due to the low concentration of Er^{3+} ions. This suggest that the decay time $1/W_{Er1}$ should not be far from this measured value. We also verified, using the rate equation model and the chosen parameter values, that the decay curve of the population N_{Er1} ($^4I_{13/2}$ state) has a lifetime close to 3 ms. Yb^{3+} ions in level 1 (see Fig. 3A) decay to the ground state with a decay time of $1/W_{Yb1} = 1$ ms. The remaining energy levels of Er^{3+} ions exhibit two contributions, a radiative decay rate to the ground state in the millisecond range ($1/W_{Er20} = 0.8$ ms, $1/W_{Er30} = 1/W_{Er40} = 0.4$ ms) and a faster nonradiative decay rate to the next lower level (partially due to multi-phonon relaxation) which is within the microsecond range. Here, we used an intrinsic quantum yield for the green level 4 (see Fig. 3A) $\eta_0 = W_{Er40}/(W_{Er40} + W_{Er43}) \simeq 0.19$, resulting in $W_{Er43} = 10^4$ s^{-1}. This value is agreement with the estimated values obtained by Bhuckory *et al.* from FRET measurements of UCNPs with different core/shell architectures.[6] For simplicity, we assumed the same value for the remaining decay rates, $W_{Er32} = W_{Er21} = W_{Er43}$ (see Fig. 3A). Furthermore, the following values for the resonant energy transfer parameters are considered. With regard to the energy transfer from Yb^{3+} to Er^{3+} ions (see Fig. 3A), we established $K_2 = 7.5 \times 10^{-17}$ cm^3 s^{-1}, with a comparable value for $K_4 = K_2$, and a lower value for the back energy transfer, $K_{B2} = 0.2K_2$. The energy transfer coefficients among neighbors Er^{3+} ions (see Fig. 3A) were set at $C_{Er1} = 0.9 \times 10^{-17}$ cm^3 s^{-1} and $C_{Er2} = 1.8 \times 10^{-17}$ cm^3 s^{-1}. The absorption cross-section of the Yb^{3+} transition at the laser wavelength is $\sigma_{Yb1} = 2 \times 10^{-21}$ cm^2. Then, the saturation intensity for the Yb^{3+} transition is $I_{sat} = 51$ kW/cm^2. To estimate the concentration of Er^{3+} (N_{Er}) and Yb^{3+} (N_{Yb}) ions, we followed the molecular weight calculation of UCNPs by Mackenzie et al.[7] We used the hexagonal crystal lattice parameters $a_h = 0.596$ nm and $c_h = 0.353$ nm to calculate the volume of a unit cell in the UCNP ($u_V \simeq 0.1086$ nm^3). Then, we took into account the fractional percentage of RE dopants f_{RE} ($RE = Yb$ and Er) to compute the RE ion concentration $N_{RE} = 1.5 f_{RE}/u_V$ ($N_{Yb} = 2.8 \times 10^{21}$ cm^{-3}, $N_{Er} = 2.8 \times 10^{20}$ cm^{-3}).

S7. Simulated UCL decay curves.

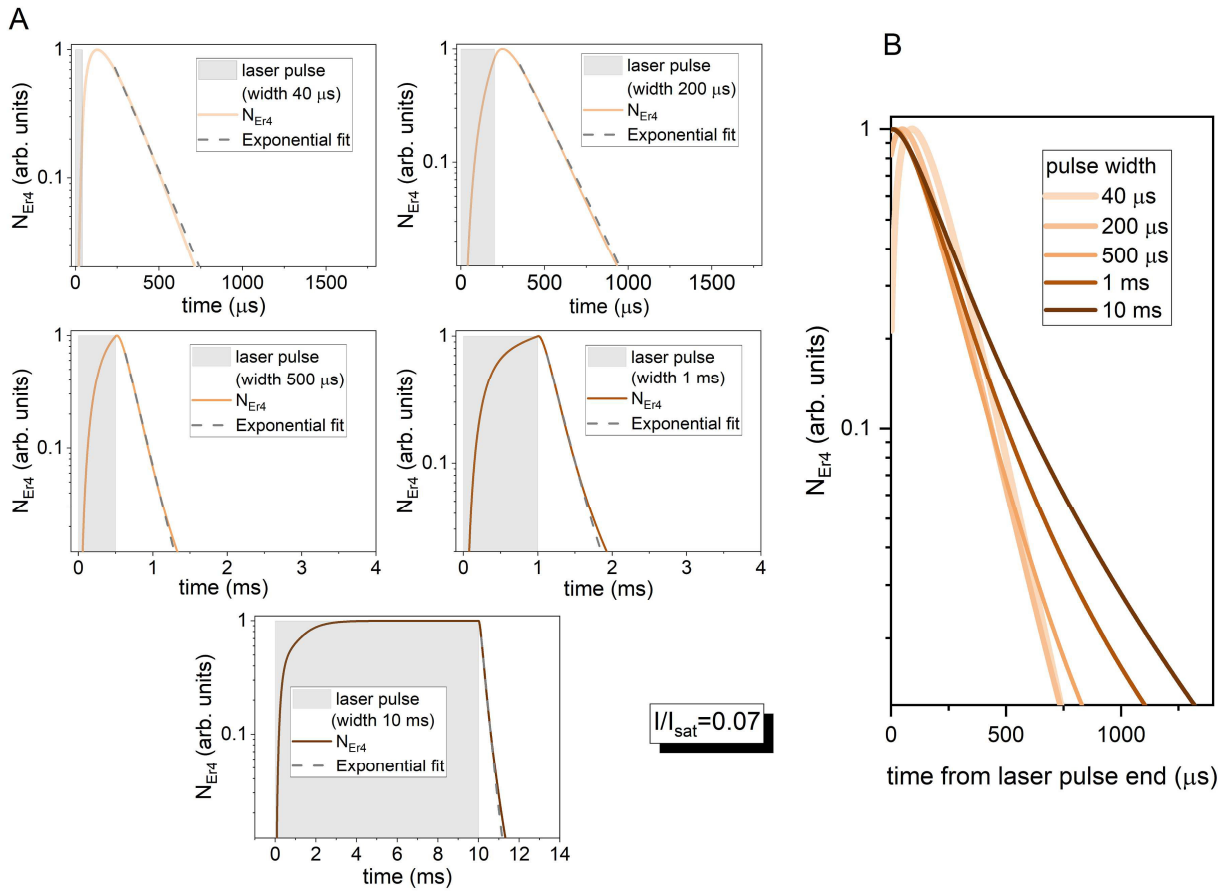

Fig. S5. (A) Temporal decay curves of the population N_{Er4} (solid lines) for various excitation pulse widths at a laser intensity $I/I_{sat} = 0.07$. The dashed lines represent exponential fitting curves. The temporal evolution of the excitation pulse is depicted with gray rectangles. (B) All the previously simulated decay curves are plotted together from the time of the end of the excitation pulse.

S8. UCNPs morphological characterization.

Table 2 Description of the UCNPs selected in Section 3.2 varying the composition of the inert shells, the nanoparticle sizes, the solvents, the matrix and adjusted the doping content of Er^{3+} and Yb^{3+} ions. Their synthesis procedures are described in detail in the provided references.

Name	Matrix	Yb^{3+} (%)	Er^{3+} (%)	Core size (nm)	Shell composition	Outer size (nm)	Solvent	Synthesis procedure
$NaYF_4$:$Yb_{0.2}$,$Er_{0.02}$@PS/PMMA	$NaYF_4$	20	2	36	75% PS, 25% PMMA	58	Water	[8]
$NaYF_4$:$Yb_{0.2}$,$Er_{0.02}$@PAA	$NaYF_4$	20	2	36	PAA		Water	[8]
$NaYF_4$:$Yb_{0.2}$,$Er_{0.02}$@SiO_2	$NaYF_4$	20	2	33	SiO_2	41	Ethanol	[9]
$NaYF_4$:$Yb_{0.07}$,$Er_{0.15}$	$NaYF_4$	7	15	30	oleate		Hexane	[10]
$SrYF_5$:$Yb_{0.90}$,$Er_{0.10}$@CaF_2	$SrYF_5$	90	10	8	CaF_2	12.5	Toluene	[11]

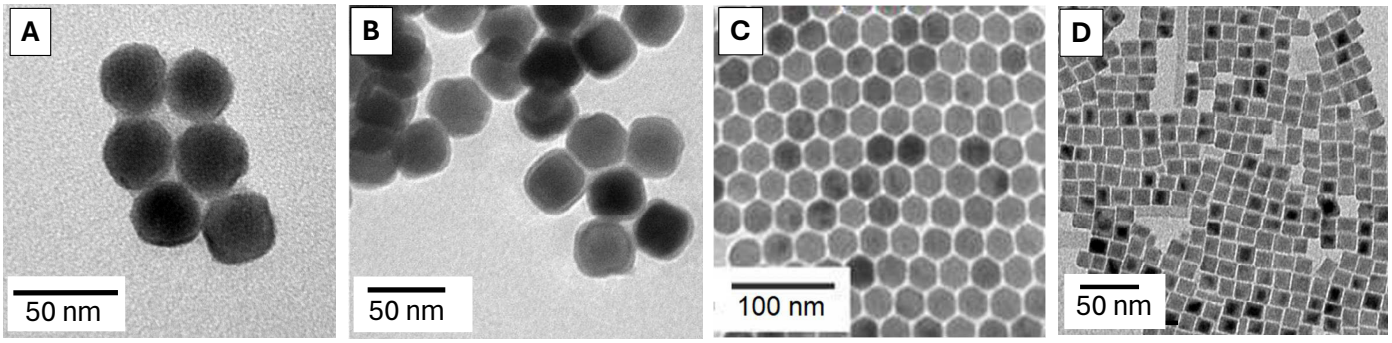

Fig. S6. TEM images of (A) $NaYF_4$:$Yb_{0.2}$,$Er_{0.02}$@PAA, (B) $NaYF_4$:$Yb_{0.2}$,$Er_{0.02}$@SiO_2, (C) $NaYF_4$:$Yb_{0.07}$,$Er_{0.15}$, (D) $SrYF_5$:$Yb_{0.90}$,$Er_{0.10}$@CaF_2.

S9. FRET efficiency with steady-state luminescence.

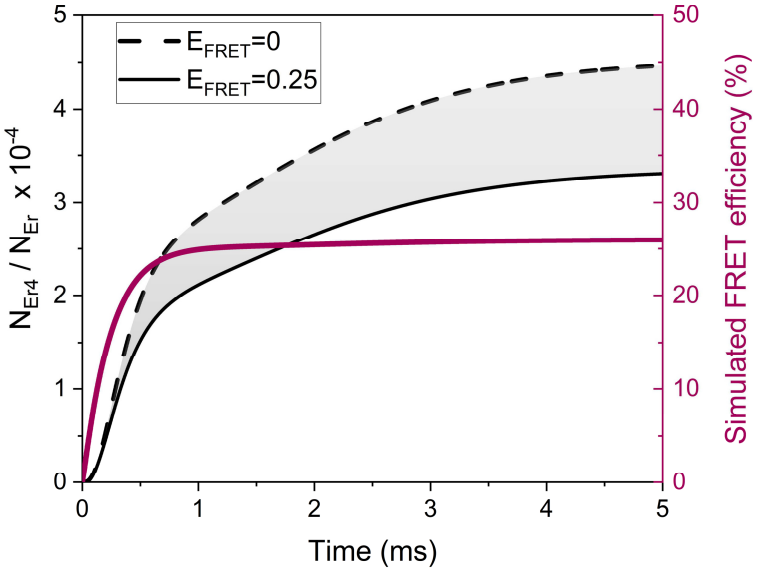

Fig. S7. (left axis) Reaching the steady state of the population of the green emission from $^4S_{3/2}$ energy level of Er^{3+} ions in the absence (black dashed line) and in the presence (black solid line) of an acceptor with a FRET efficiency of $E_{FRET} = 0.25$ ($K_{FRET} \simeq 4.4 \times 10^3$ s^{-1}). The cw laser intensity is $I = 0.025 I_{sat}$.(right axis) Using these curves we plotted the simulated FRET efficiency (pink solid line) whose steady state value agrees with the change of the decay rate of the green emission level.

References

1 L. Labrador-Páez, U. Kostiv, Q. Liu, Y. Li, H. Ågren, J. Widengren and H. Liu, *The Journal of Physical Chemistry Letters*, 2022, **13**, 11208–11215.

2 R. B. Anderson, S. J. Smith, P. S. May and M. T. Berry, *The Journal of Physical Chemistry Letters*, 2014, **5**, 36–42.

3 N. U. Wetter, A. M. Deana, I. M. Ranieri, L. Gomes and S. L. Baldochi, *IEEE Journal of Quantum Electronics*, 2010, **46**, 99–104.

4 S. Fischer, H. Steinkemper, P. Löper, M. Hermle and J. C. Goldschmidt, *Journal of Applied Physics*, 2012, **111**, 013109.

5 M. Kaiser, C. Würth, M. Kraft, T. Soukka and U. Resch-Genger, *Nano Research*, 2019, **12**, 1871–1879.

6 S. Bhuckory, E. Hemmer, Y.-T. Wu, A. Yahia-Ammar, F. Vetrone and N. Hildebrandt, *European Journal of Inorganic Chemistry*, 2017, **2017**, 5186–5195.

7 L. E. Mackenzie, J. A. Goode, A. Vakurov, P. P. Nampi, S. Saha, G. Jose and P. A. Millner, *Scientific Reports*, 2018, **8**, 1106.

8 D. Mendez-Gonzalez, V. Torres Vera, I. Zabala Gutierrez, C. Gerke, C. Cascales, J. Rubio-Retama, O. G. Calderón, S. Melle and M. Laurenti, *Small*, 2022, **18**, 2105652.

9 S. Melle, O. G. Calderon, M. Laurenti, D. Mendez-Gonzalez, A. Egatz-Gómez, E. López-Cabarcos, E. Cabrera-Granado, E. Díaz and J. Rubio-Retama, *The Journal of Physical Chemistry C*, 2018, **122**, 18751–18758.

10 V. Torres Vera, D. Mendez-Gonzalez, D. J. Ramos-Ramos, A. Igalla, M. Laurenti, R. Contreras-Caceres, E. Lopez-Cabarcos, E. Diaz, J. Rubio-Retama, S. Melle and O. G. Calderon, *Journal of Materials Chemistry C*, 2021, **9**, 8902–8911.

11 S. Fischer, C. Siefe, D. F. Swearer, C. A. McLellan, A. P. Alivisatos and J. A. Dionne, *Angewandte Chemie International Edition*, 2020, **59**, 21603–21612.